


Spin polarization and magnetotransport properties of systematically disordered Fe₆₀Al₄₀ thin filmsK. Borisov^{1,*}, J. Ehrler², C. Fowley², B. Eggert³, H. Wende³, S. Cornelius², K. Potzger², J. Lindner², J. Fassbender², R. Bali² and P. Stamenov¹¹*School of Physics, CRANN and AMBER, Trinity College, Dublin 2, Ireland*²*Institute of Ion Beam Physics and Materials Research, Helmholtz-Zentrum Dresden-Rossendorf, Bautzner Landstrasse 400, 01328 Dresden, Germany*³*Faculty of Physics and Center for Nanointegration Duisburg-Essen (CENIDE), University of Duisburg-Essen, Lotharstrasse 1, 47051 Duisburg, Germany* (Received 4 May 2021; revised 30 July 2021; accepted 13 September 2021; published 19 October 2021)

We investigate the evolution of spin polarization, spontaneous Hall angle (SHA), saturation magnetization, and Curie temperature of *B2*-ordered Fe₆₀Al₄₀ thin films under varying antisite disorder, induced by Ne⁺-ion irradiation. The spin polarization increases monotonically as a function of ion fluence. A relatively high polarization of 46% and a SHA of 3.1% are achieved on 40 nm films irradiated with 2×10^{16} ions/cm² at 30 keV. An interesting divergence in the trends of the magnetization and SHA is observed for low disorder concentrations. The high spin polarization and its broad tunability range make ion-irradiated Fe₆₀Al₄₀ a promising material for application in spin electronic devices.

DOI: [10.1103/PhysRevB.104.134417](https://doi.org/10.1103/PhysRevB.104.134417)**I. INTRODUCTION**

The performance of magnetic and electronic devices depends critically on the crystallography and chemical composition of the constituent materials. Ion irradiation is capable of modifying the magnetic properties of ordered compositions. Magnetic anisotropy direction can change from perpendicular-to-plane to in-plane upon irradiation of Co/Pt multilayers [1], while perpendicular magnetic anisotropy enhancement has been shown in FePt(001) [2]. One composition which exhibits significant sensitivity of its magnetic properties to chemical order is Fe_{1-x}Al_x. The magnetic behavior of Fe_{1-x}Al_x can be counterintuitive, in the sense that the fully ordered *B2* structure is paramagnetic (with rather low ordering temperature) while the *A2* is ferromagnetic, well above room temperature. This can be ascribed to the changes in the local environment, as treated by the crystal field model [3,4], where the average number of Fe-Fe nearest neighbors determines the strength of the exchange interaction and the magnetic moment per Fe atom. The phase region $x < 0.2$ is ferromagnetic, and the magnetization follows the linear relation $\bar{\mu} = 2.2\mu_B(1-x)/\text{Fe}$ (where μ_B is the Bohr magneton) [5]. The magnetic behavior in the intermediate-concentration region $0.2 < x < 0.4$ depends on the preparation conditions and the degree of chemical order [6–12] and is attributed to the competition between Fe-Fe ferromagnetic exchange and Fe-Al-Fe antiferromagnetic superexchange interactions.

This paper is focused on the Fe₆₀Al₄₀ alloy in thin-film form, which is paramagnetic at room temperature and is stable across a broad temperature range [7]. The ideal stoichiometric Fe₆₀Al₄₀ composition must be paramagnetic; however, antisite defects lead to finite spontaneous magnetization at low

temperature. In thin films, chemical disorder produced by ion irradiation of *B2*-ordered Fe₆₀Al₄₀ has been shown to generate ferromagnetism via the transition from the *B2* to the *A2* structure [13–15]. X-ray characterization of as-deposited and irradiated Fe₆₀Al₄₀ films has been reported before [14,16]. The ion energy can be selected such that it results in a homogeneous magnetization distribution in sufficiently thin films [17]. The transition from *B2* to *A2* has been recently exploited for embedding single nanoscale magnetic objects in a nonmagnetic matrix [18], large-area magnetic patterns [19], and reversible magnetic writing [20], as well as in tuning the magnetic anisotropy [21]. High-resolution (down to 40 nm), magnetic stripe patterning has been previously demonstrated, which opens the possibility of *writing* planar giant magnetoresistance (GMR) spin-valve structures [16]. However, properties such as the Fermi-level spin polarization $P(E_F)$, spontaneous Hall angle (SHA), and magnetoresistance (MR) are unknown.

Here, we investigate the variation of $P(E_F)$, SHA, and MR with increasing ion fluence. This paper aims to understand the scaling of relevant magnetotransport parameters with irradiation-controlled disordering. The viability of controlling $P(E_F)$ by ion irradiation is examined. We analyze in detail the MR, the SHA, and the magnetization. The behavior of the MR and SHA does not strictly follow the magnetization due to band structure modification with the lattice disordering. We show that ion irradiation can be used to significantly enhance the spin polarization. These Fe₆₀Al₄₀ thin films can be, therefore, interesting for application in spin detectors as they show large and tunable SHA.

II. EXPERIMENTAL METHODS

The samples are grown by magnetron sputtering from a single Fe₆₀Al₄₀ target onto Si(001)/SiO₂ (150 nm) substrates

*Now at GlobalFoundries; borisovk@tcd.ie

at room temperature in an Ar atmosphere of 1×10^{-3} mbar in a chamber with base pressure 1×10^{-8} mbar. The thickness of all the samples is close to 40 nm, and the samples' surfaces are not protected by a capping layer as they are self-passivating. The as-deposited thin films are annealed at 500 °C in a high-vacuum furnace with base pressure 5×10^{-7} mbar for 1 h in order to form the ordered B_2 phase. Irradiation was performed with Ne^+ ions with energy 30 keV at the Ion Beam Center (IBC), Helmholtz-Zentrum Dresden-Rossendorf (HZDR). The thicknesses of the films are measured by x-ray reflectivity (XRR). All magnetotransport measurements are performed on blanket films in van der Pauw geometry in a Quantum Design Physical Property Measurement System (PPMS) with the standard resistivity option or with Keithley 2400 source meter units in the temperature range of 10–300 K and applied field of up to $\mu_0 H = \pm 14$ T. The anomalous Hall effect (AHE) and MR are calculated from the raw Hall effect data (ρ_{xy}) after field antisymmetrization and field symmetrization:

$$\text{AHE}(\mu_0 H) = [\rho_{xy}(\mu_0 H) - \rho_{xy}(-\mu_0 H)]/2,$$

$$\text{MR}(\mu_0 H) = [\rho_{xy}(\mu_0 H) + \rho_{xy}(-\mu_0 H)]/2.$$

The SHA is determined by normalizing the amplitude of the AHE with the longitudinal resistivity (ρ_{xx}). Point contact Andreev reflection (PCAR) lock-in-based differential conductance $G(V)$ spectroscopy is performed using a superconducting Nb tip within a purpose-built electrical insert in the PPMS, at $T = 2.0$ K. The analysis is done within the modified Blonder-Tinkham-Klapwijk model (mBTK) [22,23]. A comprehensive description of the data acquisition, processing, and fitting routines is given elsewhere [22,24,25]. Each thin film is gently cleaned with low-energy Ar plasma (300 W/dm², incident at 30° to the surface) before PCAR measurement, in order to remove the passivation surface oxide layer, and then swiftly transferred to the measurement cryostat. Magnetometry is measured in a Quantum Design Magnetic Property Measurement System (MPMS) at $T = 4$ –300 K with the reciprocating sample option (RSO) and at higher temperatures from 300 to 700 K with the oven insert. Further measurements are provided in the Supplemental Material [26].

III. EXPERIMENTAL RESULTS

A. Magnetometry

First we demonstrate the changes in the saturation magnetization and the Curie temperature with increasing disorder (Fig. 1). Thermal diffusion can result in reordering of the films during the $M(T)$ measurement, and for this reason these measurements were performed last. The saturation magnetization demonstrates consistent increase as a function of the irradiation fluence: from 20 kA/m for the well-ordered B_2 $\text{Fe}_{60}\text{Al}_{40}$ film [16] to 800 kA/m (for fluence of 2×10^{16} ions/cm²). The magnetocrystalline anisotropy K_1 is extracted from the apparent anisotropy field after the demagnetizing field correction. This results in $K_1 = 50$ kJ/m³ (for 6×10^{14} ions/cm²) and $K_1 = 14$ kJ/m³ (for 2×10^{16} ions/cm²). The magnetocrystalline anisotropy is small (as expected for a cubic structure) and for the lowest fluence sample is close to the value of bulk αFe [110] [27]. The magnetic response difference between the

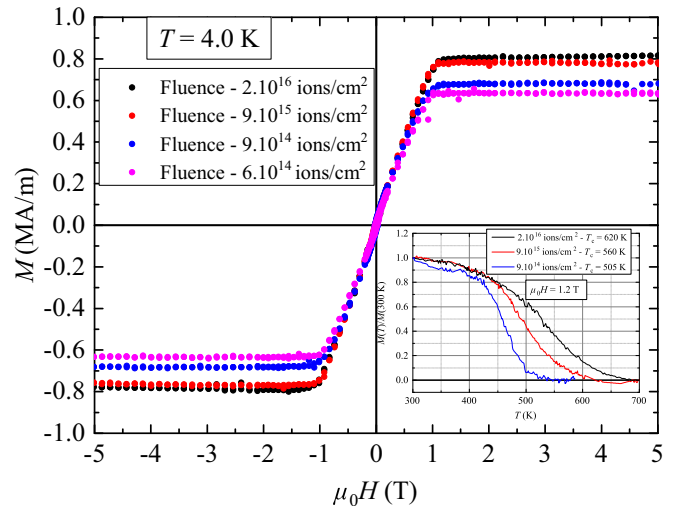


FIG. 1. Hysteresis curves of four samples with different irradiation fluences, measured at 4 K, with the magnetic field applied perpendicular to the plane. Inset: Curie temperature measurements of three samples with different irradiation fluences with in-plane magnetic field $\mu_0 H = 1.2$ T.

B_2 and A_2 films is studied also by Mössbauer depth profile spectroscopy in Fig. S3 of the Supplemental Material [26].

The Curie temperature is shown to increase with the irradiation fluence from $T_C \approx 505$ K for 9×10^{14} ions/cm² to 620 K for 2×10^{16} ions/cm² (see inset of Fig. 1). There is a positive correlation between the irradiation fluence and the Curie temperature enhancement as is the case with the saturation magnetization.

B. Spin polarization measurements

Fermi-level spin polarization $P(E_F)$ is investigated in samples with different irradiation fluences by the well-established PCAR technique [28]. The spin polarization of five samples—the as-deposited composition and four with different irradiation fluences of up to 2×10^{16} ions/cm²—is measured. Representative PCAR spectra along with mBTK fits on the B_2 -ordered sample and the A_2 -ordered one with the highest irradiation fluence are plotted in Figs. 2(a) and 2(b), respectively, where the extracted parameters from the analysis are the superconducting proximity gap Δ_1^* , barrier strength Z^* , spin polarization P^* , and effective electron temperature T_e^* . The nonirradiated sample demonstrates an increased zero-bias conductance, which is indicative of a very low spin polarization [28]. The fitted value of $P \approx 10\%$ shows that the B_2 -ordered sample has no appreciable spin polarization at E_F , while the significant error (10%) is because of PCAR's low sensitivity at small P values [31]. Furthermore, four samples with increasing irradiation fluences are investigated. The spin polarization has been extracted to be 25(3), 26(3), 40(6), and 46(3)% for irradiation fluences of 6×10^{14} , 2×10^{15} , 9×10^{15} , and 2×10^{16} ions/cm², respectively. The trend towards higher spin polarization signifies a positive correlation between the irradiation fluence and the difference between the spin-up and spin-down density of states (DOS) at the Fermi level. Further insight into the properties of the band structure

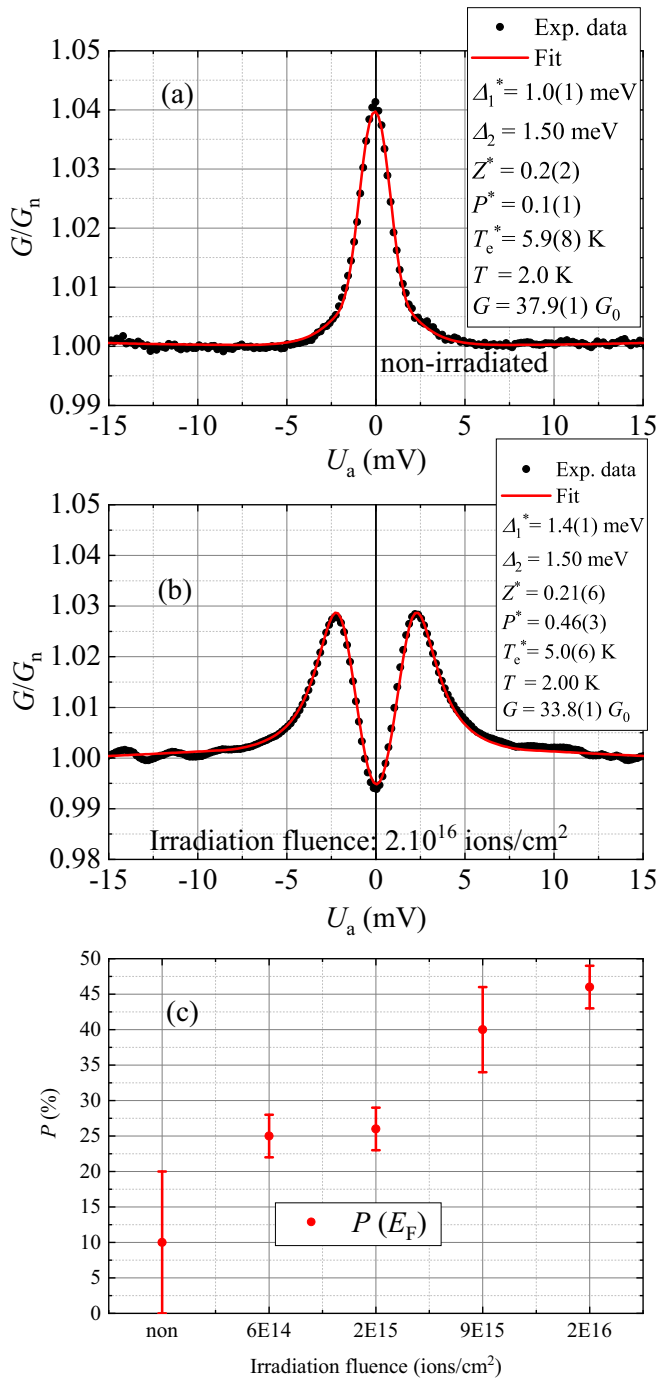


FIG. 2. PCAR spin polarization measurements of $\text{Fe}_{60}\text{Al}_{40}$ thin films with different irradiation fluences. The values are evaluated within the ballistic transport regime due to the high point contact resistance in these measurements [29,30]. (a) PCAR of a nonirradiated sample with small spin polarization of $P \approx 10\%$. (b) PCAR of a sample irradiated with the highest fluence of 2×10^{16} ions/cm² with moderately high spin polarization $P \approx 46(3)\%$. An asterisk superscript indicates fitted parameters. (c) Spin polarization values as a function of the irradiation fluence.

at the Fermi level is given by the magnetotransport behavior of the irradiated films.

C. Nonsaturating spontaneous Hall angle

We have measured significant disagreement between the SHA and the magnetization of the irradiated $\text{Fe}_{60}\text{Al}_{40}$ samples [32]. The latter is most striking for the sample with the low irradiation fluence of 6×10^{14} ions/cm² [see Figs. 3(a) and 3(b)]. Neither the low-temperature SHA nor the room-temperature SHA reaches saturation at 14 T in contrast to the superconducting quantum interference device (SQUID) magnetization for this sample. For the highest irradiation fluence, SHA is essentially saturated beyond $\mu_0 H_{\text{an}} \approx 1.1$ T [Fig. 3(c)] as is the bulk magnetization [Fig. 3(d)] at 10 K. Interestingly, there is a pronounced discrepancy between the SHA and SQUID magnetometry beyond $\mu_0 H_{\text{an}}$ at 300 K. The SHA exhibits an inflection point at $\mu_0 H_{\text{an}}$; however, the high-field signal does not reach saturation even at 14 T [see red curve in Fig. 3(c)]. The room-temperature SHA clearly has a nonlinear character and hence is attributed to the anomalous Hall effect and not to the ordinary Hall effect, i.e., change in the carrier density between 10 and 300 K (the ordinary Hall effect must be linear). The change in the high-field background beyond 1 T ($\mu_0 H_{\text{an}}$) evolves smoothly from a flat line (highest fluence) to a quasiquadratic, nonsaturating background (lowest fluence).

D. Magnetoresistance

The magnetoresistance (MR) of the samples with the highest and the lowest irradiation fluences at various temperatures is presented in Figs. 4(a) and 4(b). The MR of the highest-irradiation-fluence sample changes from negative to positive between 10 and 300 K, which can indicate change in the dominant carrier type (for the most mobile bands). A pronounced increase in MR amplitude is seen at 300 K which coincides with the nonsaturating Hall effect at the same temperature [see Fig. 3(c)]. On the other hand, the sample with an irradiation fluence of 6×10^{14} ions/cm² exhibits constant positive magnetoresistance at all measured temperatures and hence confirms a constant carrier type which is temperature independent [Fig. 4(b)]. The MR and Hall effect of the highest-fluence sample are fitted within a two-carrier-type model at 10 and 300 K [33,34] in Figs. 4(c)–4(f). The model assumes multiple carrier types with effective masses equal to the free-electron mass; therefore negative n_i means effective mass with opposite sign ($i = 2$)—a hole. At low temperature, the first carrier type has concentration $n_1(10 \text{ K}) = 2.328 \times 10^{27} \text{ m}^{-3}$ and scattering time $\tau_1(10 \text{ K}) = 2.24 \times 10^{-13} \text{ s}$, while the second carrier type has concentration $n_2(10 \text{ K}) = -2.213 \times 10^{29} \text{ m}^{-3}$ and scattering time $\tau_2(10 \text{ K}) = 2.71 \times 10^{-14} \text{ s}$. On the other hand, at room temperature, the first carrier type has $n_1(300 \text{ K}) = 1.37 \times 10^{29} \text{ m}^{-3}$ and $\tau_1(300 \text{ K}) = 7.28 \times 10^{-14} \text{ s}$, while the second carrier type has $n_2(300 \text{ K}) = -1.54 \times 10^{28} \text{ m}^{-3}$ and $\tau_2(300 \text{ K}) = 2.81 \times 10^{-13} \text{ s}$. The extracted higher concentration of holes at low temperature confirms the already anticipated result from the negative MR. We can estimate the conductivity contributions, $\sigma_i = n_i e \mu_i$ with the mobility $\mu_i = e \tau_i / m_e$, where e and m_e are the electron's charge and mass. It is evident that $|\sigma_1^e(10 \text{ K})| < |\sigma_2^h(10 \text{ K})|$, which confirms the dominant conductivity contribution of holes at low temperature. In contrast, $|\sigma_1^e(300 \text{ K})| > |\sigma_2^h(300 \text{ K})|$,

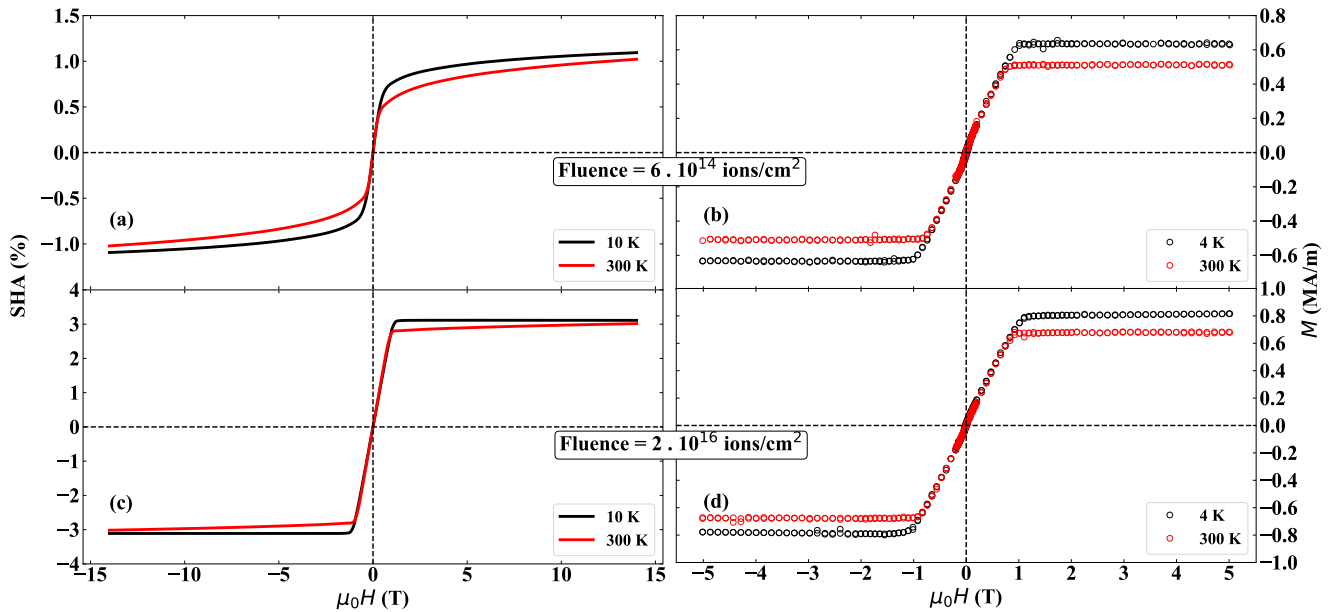


FIG. 3. Comparison between the SHA and SQUID magnetometry on a sample with low irradiation fluence (6×10^{14} ions/cm²) and high irradiation fluence (2×10^{16} ions/cm²). The magnetic field is always applied perpendicular to the sample plane. (a) SHA measurement at 10 and 300 K for the low-irradiation-fluence sample. (b) Magnetization data at 4 and 300 K for the same sample. (c) SHA measurement at 10 and 300 K for the high-irradiation-fluence sample. (d) Magnetization data at 4 and 300 K for the same sample.

which testifies to the dominant conductivity contribution of electrons at room temperature. An analogous carrier type crossover was recently reported for other transition metal

alloys [35]. The constancy of the dominating carrier type for the low-irradiation-fluence sample is corroborated within the two-carrier-type analysis. No other sample exhibited MR

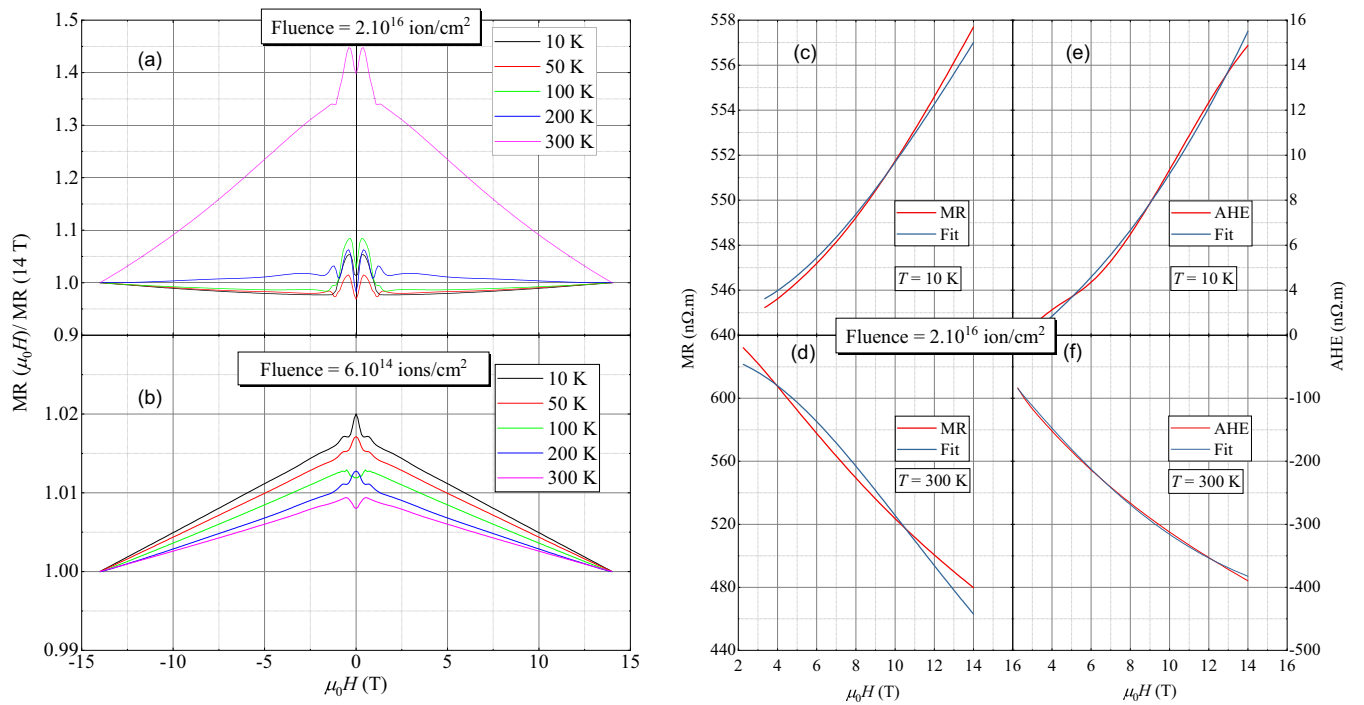


FIG. 4. Two-carrier-type analysis of magnetoresistance and AHE of the highest-irradiation-fluence sample (2×10^{16} ions/cm²). (a) MR of sample with irradiation fluence 2×10^{16} ions/cm² at various temperatures. (b) MR of sample with irradiation fluence 6×10^{14} ions/cm² at various temperatures. The V-shaped feature at low field is an antisymmetrization artifact. (c) and (d) MR of the high-fluence samples at 10 and 300 K along with two-carrier-type model fits. (e) and (f) AHE of the high-fluence samples at 10 and 300 K along with two-carrier-type model fits.

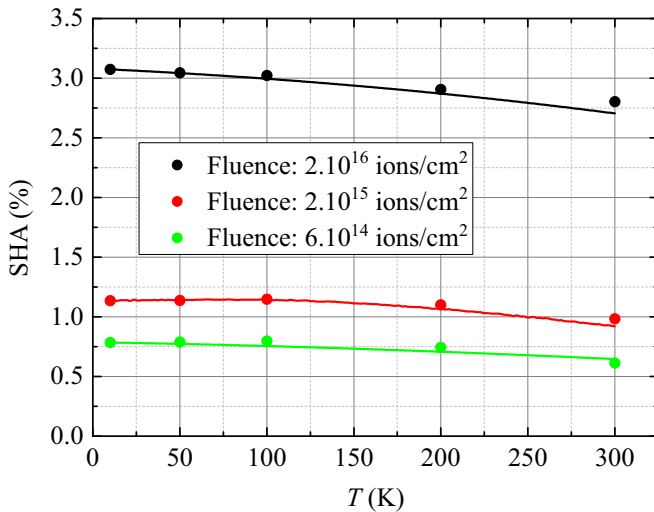


FIG. 5. Comparison between the magnetization and SHA temperature dependence for three samples with different irradiation fluences. The solid circles represent the SHA. The solid curves are the magnetization data, which have been normalized to the SHA (10 K) for each sample. The magnetization and SHA signals are taken at 1.2 T. See Fig. S2 of the Supplemental Material [26] for further details.

sign change for $T = 10$ –300 K apart from the maximum-irradiation-fluence one. The curvature of the high-field data does not allow a proper fitting with more than two carrier types and resulted in nonphysical results.

E. Temperature dependence of spontaneous Hall angle

A comparison between the normalized magnetization and the normalized SHA for three irradiation fluences is presented in Fig. 5. The irradiation dependence shows that SHA equals 0.7% for 6×10^{14} ions/cm², increases to 1.1% for 2×10^{15} ions/cm², and reaches 3.1% for the sample irradiated with 2×10^{16} ions/cm². Similar SHA values have been recently reproduced by first-principles calculation on the disorder effect in Fe₆₀Al₄₀ [36]. High SHA values, within the same order of magnitude, have been reported in amorphous Fe_{0.79}Gd_{0.21} (5.8%) [37], amorphous Co-Tb (3.2%) [38], L1₀-FePt (3.3%) [39], Mn-Ga (5.7%) [40], Mn₂Ru_xGa (7.7%) [41], and amorphous Co₄₀Fe₄₀B₂₀ (2.3%) [42].

F. Discussion

The magnetometry data in Fig. 1 demonstrate an increase in the saturation magnetization M_s as a function of the irradiation fluence, which is consistent with growing antisite disorder. The M_s reaches 800 kA/m for the highest irradiation fluence of 2×10^{16} ions/cm². In accordance with M_s , the Curie temperature is determined to increase as well, up to 620 K for the highest fluence. Structural reordering towards the B2 phase is reported to commence at ≈ 400 K [43]. This occurs simultaneously with the Curie transition and further lowers the magnetization.

The PCAR measurements (see Fig. 2) demonstrate a pronounced enhancement of the Fermi-level spin polarization from very low (10%) for the nonirradiated sample to a

respectably high value (46%) for the highest irradiation fluence of 2×10^{16} ions/cm². Higher spin polarization implies stronger s - d exchange interaction, which is in line with the higher Curie temperatures of the more irradiated compositions (see inset of Fig. 1). The measured Fermi-level spin polarization of up to 46(3)% is similar to the value of pure Fe [44] and close to the value of the exemplary high-moment Co-Fe compositions [44,45].

The comparison between the SQUID magnetometry and the AHE measurements evidenced in Fig. 3 shows an intriguing disagreement. A viable explanation is that the splitting of the s bands is influenced by the irradiation fluence and temperature. The conduction process is dominated by the more mobile s electrons with the accompanying spin splitting of the s density of states, while the bulk magnetization is determined by the splitting of the d states. The latter implies essentially that the s - d coupling, through which the conduction electrons become spin polarized, is smaller for the samples irradiated with lower fluence. Hence the nonsaturating AHE contribution is attributed to nonpolarized (random spin orientation), Al-related s bands. For low irradiation fluences, these bands have a high contribution to the Fermi-level transport. The Fe s bands are not sufficiently split in this case (compared with those in α Fe), and they are responsible for the AHE signal up to $\mu_0 H_{an}$. For $\mu_0 H > \mu_0 H_{an}$, the magnetic field acts on the Al s electrons, their spins are gradually more aligned with the sample magnetization direction, and this leads to the AHE increasing in magnitude up to and above 14 T. For higher irradiation fluences, the two Fe s bands are more strongly split, and one of them dominates the Fermi-level transport. This makes the Al s -band contribution small and can explain why the AHE behavior closely follows the magnetization [low temperature in Figs. 3(c) and 3(d)]. For the highest fluence at room temperature, thermal activation reduces the effective Fe s -band splitting (i.e., spin polarization), and this allows the Al s bands to exhibit their small, nonsaturating contribution [300 K in Fig. 3(c)]. Therefore our interpretation is that the irradiation modifies the effective s - d coupling strength and governs the Fe s -band splitting for this composition. This conjecture is in line with the PCAR data, presented in Fig. 2, which demonstrates that the lower-fluence samples have lower spin polarization and therefore smaller spin splitting for the conduction bands. Further resistivity measurements are provided in the Supplemental Material (Fig. S1) [26].

The temperature evolution of the magnetoresistance supports this argument (Fig. 4). For the highest irradiation fluence (2×10^{16} ions/cm²), the MR changes sign at $T \approx 150$ K ($\Delta E \approx 15$ meV). This observation can be explained by the temperature-dependent Fermi level, which shifts position between distinct density-of-states structures, which are attributable to different carrier types, with energy spacing of the order of ΔE [see Fig. 4(a)]. The latter is confirmed within a two-carrier model fitting of the MR and the AHE [Figs. 4(c)–4(f)]. The low-temperature MR sign change from positive to negative, as the number of Fe-Fe nearest neighbors increases due to irradiation, is reproduced by electronic structure calculations [36].

The comparison between the normalized magnetization's and the SHA's temperature decrease shows similar behavior and a similar small reduction for all samples from 10 to 300 K

[46] (Fig. 5). The latter is a strong point that magnetotransport properties vary weakly with temperature, which is an important material prerequisite for integration in spin electronic devices. Most prominent is the SHA temperature decrease for the highest fluence, which is significantly smaller than the magnetization reduction (see black curve in Fig. 5). This indicates that the spin polarization depends on a complicated spin-split density-of-states structure close to E_F . This observation may open new pathways for engineering spin transport in this composition. The Fermi-level spin polarization $P(E_F)$ may increase further in this A2-ordered alloy despite the fact that the value of Fe is already reached, because it is the DOS contributions of both Fe and Al bands and their hybridization which determine $P(E_F)$ in $\text{Fe}_{60}\text{Al}_{40}$.

IV. CONCLUSION

The spin polarization, spontaneous Hall angle, saturation magnetization, and Curie temperature are shown to increase in $\text{Fe}_{60}\text{Al}_{40}$ thin films upon B2-A2 crystal structure transition induced by irradiation with Ne^+ ions. For an irradiation fluence of 2×10^{16} ions/cm², the spin polarization reaches 46(3)%, the spontaneous Hall angle reaches 3.1%, and the Curie temperature reaches 620 K. Ion irradiation is demonstrated as an efficient method to increase the spin polarization and to modify the *s-d* splitting in thin $\text{Fe}_{60}\text{Al}_{40}$ films. The discrepancy between the high-field nonsaturating anomalous Hall effect and the magnetization is attributed to a high electrical transport contribution from nonpolarized, aluminium-related bands for low irradiation fluences. Such AHE-magnetization disagreement could be taken as an indication of lower spin polarization. Even though it is possible to account for some of the observed discrepancy between the magnetization and the AHE as being due to the suppression of the topological Hall effect present in the B2-ordered phase, the level of difference in electron-phonon scattering observed between the highest and lowest irradiation fluences, for which the room-

temperature saturation magnetization is properly developed, does not seem to be corroborated to the same extent as for the dominant contribution. In view of this, it seems likely that, in other intermetallic systems with weak anisotropy and large saturation moment, the reported differences between the apparent approaches to saturation, as seen in the magnetization and the Hall effect, may have other explanations besides the topological Hall effect.

The measured spin polarization of 46% implies that such irradiated compositions can be used as spin injectors or detectors in GMR spin valves and novel magnetic circuit designs. Spin diffusion length measurements of a nonirradiated sample and the energy dependence of the spin-split density of states of irradiated samples could be interesting future research directions, which would help optimize the irradiation and annealing strategies. The irradiation-induced ferromagnetic state in $\text{Fe}_{60}\text{Al}_{40}$ with the accompanying beneficial magnetotransport properties gives this composition the potential for integration in novel magnetic device geometries with high design flexibility and reduced processing complexity.

ACKNOWLEDGMENTS

K.B. and P.S. would like to acknowledge financial support from Science Foundation Ireland within SSPP (Grant No. 11/SIRG/I2130), NISE (Grant No. 10/IN1/I3002), and the AMBER program (Grant No. 12/RC/2278). R.B. and H.W. acknowledge funding by the Deutsche Forschungsgemeinschaft (DFG) - 322462997 (Grants No. BA 5656/1-2 and No. WE 2623/14-2). K.B., C.F., and P.S. acknowledge support within the European Union Horizon 2020 research and innovation program under Grant Agreement No. DLV-737038 (TRANSPiRE). Support by the Ion Beam Center (IBC) at HZDR is gratefully acknowledged. We are thankful to Prof. J. M. D. Coey, Dr. M. Venkatesan, Dr. P. Tozman, and Dr. S. Khmelevskiy for fruitful discussions.

-
- [1] C. Chappert, H. Bernas, J. Ferré, V. Kottler, J.-P. Jamet, Y. Chen, E. Cambriil, T. Devolder, F. Rousseaux, V. Mathet, and H. Launois, *Science* **280**, 1919 (1998).
 - [2] D. Ravelosona, C. Chappert, V. Mathet, and H. Bernas, *J. Appl. Phys. (Melville, NY)* **87**, 5771 (2000).
 - [3] G. K. Wertheim, V. Jaccarino, J. H. Wernick, and D. N. E. Buchanan, *Phys. Rev. Lett.* **12**, 24 (1964).
 - [4] S. Takahashi, *J. Magn. Magn. Mater.* **54**, 1065 (1986).
 - [5] G. A. P. Alcazar and E. G. da Silva, *J. Phys. F: Met. Phys.* **17**, 2323 (1987).
 - [6] R. Bernal-Correa, A. Rosales-Rivera, P. Pineda-Gómez, and N. Salazar, *J. Alloys Compd.* **495**, 491 (2010).
 - [7] A. Taylor and R. Jones, *J. Phys. Chem. Solids* **6**, 16 (1958).
 - [8] E. Yelsukov, E. Voronina, and V. Barinov, *J. Magn. Magn. Mater.* **115**, 271 (1992).
 - [9] H. Sato and A. Arrott, *Phys. Rev.* **114**, 1427 (1959).
 - [10] I. Vincze, *Phys. Status Solidi A* **7**, K43 (1971).
 - [11] R. Shull, H. Okamoto, and P. Beck, *Solid State Commun.* **20**, 863 (1976).
 - [12] M. Shiga and Y. Nakamura, *J. Phys. Soc. Jpn.* **40**, 1295 (1976).
 - [13] E. Menéndez, M. O. Liedke, J. Fassbender, T. Gemming, A. Weber, L. J. Heyderman, K. V. Rao, S. C. Deevi, S. Suriñach, M. D. Baró, J. Sort, and J. Nogués, *Small* **5**, 229 (2009).
 - [14] E. La Torre, A. Smekhova, C. Schmitz-Antoniak, K. Ollefs, B. Eggert, B. Cöster, D. Walecki, F. Wilhelm, A. Rogalev, J. Lindner, R. Bali, R. Banerjee, B. Sanyal, and H. Wende, *Phys. Rev. B* **98**, 024101 (2018).
 - [15] J. Ehrler, B. Sanyal, J. Grenzer, S. Zhou, R. Böttger, B. Eggert, H. Wende, J. Lindner, J. Fassbender, C. Leyens, K. Potzger, and R. Bali, *New J. Phys.* **22**, 073004 (2020).
 - [16] R. Bali, S. Wintz, F. Meutzner, R. Hübner, R. Boucher, A. A. Ínal, S. Valencia, A. Neudert, K. Potzger, J. Bauch, F. Kronast, S. Facsco, J. Lindner, and J. Fassbender, *Nano Lett.* **14**, 435 (2014).
 - [17] F. Röder, G. Hlawacek, S. Wintz, R. Hübner, L. Bischoff, H. Lichte, K. Potzger, J. Lindner, J. Fassbender, and R. Bali, *Sci. Rep.* **5**, 16786 (2015).
 - [18] M. Nord, A. Semisalova, A. Kákay, G. Hlawacek, I. MacLaren, V. Liersch, O. M. Volkov, D. Makarov, G. W. Paterson, K. Potzger, J. Lindner, J. Fassbender, D. McGrouther, and R. Bali, *Small* **15**, 1904738 (2019).

- [19] M. Krupinski, R. Bali, D. Mitin, P. Sobieszczyk, J. Gregor-Pawłowski, A. Zarzycki, R. Böttger, M. Albrecht, K. Potzger, and M. Marszałek, *Nanoscale* **11**, 8930 (2019).
- [20] J. Ehrler, M. He, M. V. Shugaev, N. I. Polushkin, S. Wintz, V. Liersch, S. Cornelius, R. Hübner, K. Potzger, J. Lindner, J. Fassbender, A. A. Ínal, S. Valencia, F. Kronast, L. V. Zhigilei, and R. Bali, *ACS Appl. Mater. Interfaces* **10**, 15232 (2018).
- [21] T. Schneider, K. Lenz, A. Semisalova, J. Gollwitzer, J. Heitler-Klevans, K. Potzger, J. Fassbender, J. Lindner, and R. Bali, *J. Appl. Phys. (Melville, NY)* **125**, 195302 (2019).
- [22] G. J. Strijkers, Y. Ji, F. Y. Yang, C. L. Chien, and J. M. Byers, *Phys. Rev. B* **63**, 104510 (2001).
- [23] G. E. Blonder, M. Tinkham, and T. M. Klapwijk, *Phys. Rev. B* **25**, 4515 (1982).
- [24] P. Stamenov, *J. Appl. Phys. (Melville, NY)* **111**, 07C519 (2012).
- [25] K. Borisov, C.-Z. Chang, J. S. Moodera, and P. Stamenov, *Phys. Rev. B* **94**, 094415 (2016).
- [26] See Supplemental Material at <http://link.aps.org/supplemental/10.1103/PhysRevB.104.134417> for additional information on resistance-temperature behavior [16,47–57], spontaneous Hall angle, and Mössbauer depth profile spectroscopy of Ne⁺-ion-irradiated Fe₆₀Al₄₀ thin films [14,58,59].
- [27] H. Lawton and K. H. Stewart, *Proc. R. Soc. London, Ser. A* **193**, 72 (1948).
- [28] R. J. Soulen Jr., M. S. Osofsky, B. Nadgorny, T. Ambrose, P. Broussard, S. F. Cheng, J. Byers, C. T. Tanaka, J. Nowack, J. S. Moodera, G. Laprade, A. Barry, and M. D. Coey, *J. Appl. Phys. (Melville, NY)* **85**, 4589 (1999).
- [29] I. I. Mazin, A. A. Golubov, and B. Nadgorny, *J. Appl. Phys. (Melville, NY)* **89**, 7576 (2001).
- [30] J. Gramich, P. Brenner, C. Sürgers, H. v. Löhneysen, and G. Goll, *Phys. Rev. B* **86**, 155402 (2012).
- [31] Y. Bugoslavsky, Y. Miyoshi, S. K. Clowes, W. R. Branford, M. Lake, I. Brown, A. D. Caplin, and L. F. Cohen, *Phys. Rev. B* **71**, 104523 (2005).
- [32] N. Nagaosa, J. Sinova, S. Onoda, A. H. MacDonald, and N. P. Ong, *Rev. Mod. Phys.* **82**, 1539 (2010).
- [33] J. Alaria, Magnetic semiconductors for spin electronics, Ph.D. thesis, Trinity College Dublin, College Green, Dublin 2, Ireland, 2009, <http://www.tara.tcd.ie/handle/2262/77846>.
- [34] K. Borisov, J. Alaria, J. M. D. Coey, and P. Stamenov, *J. Appl. Phys. (Melville, NY)* **115**, 17C717 (2014).
- [35] T. da Câmara Santa Clara Gomes, N. Marchal, F. Abreu Araujo, and L. Piraux, *Appl. Phys. Lett.* **115**, 242402 (2019).
- [36] J. Kudrnovský, V. Drchal, F. Máca, I. Turek, and S. Khmelevskiy, *Phys. Rev. B* **101**, 054437 (2020).
- [37] T. R. McGuire, R. J. Gambino, and R. C. Taylor, *J. Appl. Phys. (Melville, NY)* **48**, 2965 (1977).
- [38] T. W. Kim and R. J. Gambino, *J. Appl. Phys. (Melville, NY)* **87**, 1869 (2000).
- [39] J. Yu, U. Ruediger, A. D. Kent, R. F. C. Farrow, R. F. Marks, D. Weller, L. Folks, and S. S. P. Parkin, *J. Appl. Phys. (Melville, NY)* **87**, 6854 (2000).
- [40] F. Wu, E. P. Sajitha, S. Mizukami, D. Watanabe, T. Miyazaki, H. Naganuma, M. Oogane, and Y. Ando, *Appl. Phys. Lett.* **96**, 042505 (2010).
- [41] N. Thiagarajah, Y.-C. Lau, D. Betto, K. Borisov, J. M. D. Coey, P. Stamenov, and K. Rode, *Appl. Phys. Lett.* **106**, 122402 (2015).
- [42] G. Su, Y. Li, D. Hou, X. Jin, H. Liu, and S. Wang, *Phys. Rev. B* **90**, 214410 (2014).
- [43] J. Ehrler, M. O. Liedke, J. Čížek, R. Boucher, M. Butterling, S. Zhou, R. Böttger, E. Hirschmann, T. T. Trinh, A. Wagner, J. Lindner, J. Fassbender, C. Leyens, K. Potzger, and R. Bali, *Acta Mater.* **176**, 167 (2019).
- [44] S. V. Karthik, T. M. Nakatani, A. Rajanikanth, Y. K. Takahashi, and K. Hono, *J. Appl. Phys. (Melville, NY)* **105**, 07C916 (2009).
- [45] S. S. P. Parkin, C. Kaiser, A. Panchula, P. M. Rice, B. Hughes, M. Samant, and S.-H. Yang, *Nat. Mater.* **3**, 862 (2004).
- [46] L. Ye, Y. Tian, X. Jin, and D. Xiao, *Phys. Rev. B* **85**, 220403(R) (2012).
- [47] L. Bainsla, K. G. Suresh, A. K. Nigam, M. M. Raja, B. S. D. C. S. Varaprasad, Y. K. Takahashi, and K. Hono, *J. Appl. Phys.* **116**, 203902 (2014).
- [48] D. Betto, Y.-C. Lau, K. Borisov, K. Kummer, N. B. Brookes, P. Stamenov, J. M. D. Coey, and K. Rode, *Phys. Rev. B* **96**, 024408 (2017).
- [49] J. H. Mooij, *Physica Status Solidi (a)* **17**, 521 (1973).
- [50] M. Gurvitch, *Phys. Rev. B* **24**, 7404 (1981).
- [51] R. W. Houghton, M. P. Sarachik, and J. S. Kouvel, *Phys. Rev. Lett.* **25**, 238 (1970).
- [52] H. M. Ahmad and D. Greig, *Phys. Rev. Lett.* **32**, 833 (1974).
- [53] F. Goedsche, R. Richter, and A. Richter, *Physica Status Solidi (b)* **69**, 213 (1975).
- [54] F. Brouers and M. Brauwiers, *Solid State Commun.* **25**, 785 (1978).
- [55] P. R. Wallace, *Phys. Rev.* **71**, 622 (1947).
- [56] J. W. McClure, *J. Low Temp. Phys.* **25**, 527 (1976).
- [57] C. Kaiser, G. Weiss, T. W. Cornelius, M. E. Toimil-Molares, and R. Neumann, *J. Phys.: Condens. Matter* **21**, 205301 (2009).
- [58] M. O. Liedke, W. Anwand, R. Bali, S. Cornelius, M. Butterling, T. T. Trinh, A. Wagner, S. Salamon, D. Walecki, A. Smekhova, H. Wende, and K. Potzger, *J. Appl. Phys.* **117**, 163908 (2015).
- [59] L. Cser, J. Ostauvech, and L. Pal, *Physica Status Solidi (b)* **20**, 581 (1967).